Xia Yuhui
Li Chenggang
You Jingjing
Shen Jingjin
Jason Zachary Moore

INFLUENCES ANALYSIS OF CONFIGURATIONS ON THE PERFORMANCE OF PARALLEL TYPE SIX-AXIS ACCELEROMETERS

Summary

The development of parallel type six-axis accelerometers was hindered for their complicated forward kinematics and dynamics algorithms which make it difficult to decouple the six acceleration components timely, accurately and stably. This paper applies four parallel configurations with 6-DOF and a closed-form solution of the forward kinematics to six-axis accelerometers as the elastic bodies, where the piezoelectric ceramics act as the sensitive elements and play the role of prismatic pairs. An efficient decoupling algorithm was derived to calculate the six acceleration components completely by the use of Kane's dynamics method in configuration space. Considering the differences in sensing properties of the four six-axis accelerometers, a quantitative comparison was conducted to reveal the configurations' direct influences on some static characteristics, including accuracy, efficiency, sensitivity, isotropy, and working frequency range, which makes a theoretical foundation for the subsequent design of a reconfigurable prototype.

Key words: *six-axis accelerometer, parallel configuration, decoupling algorithm, static characteristics*

1. Introduction

Six-axis acceleration sensing technology, a multidimensional motion sensing technology, is used to simultaneously sense and measure all three linear acceleration components a_x, a_y, a_z and three angular acceleration components α_x, α_y, α_z of a rigid body with a six-dimensional movement relative to the inertial reference system. The state of motion of a body can be accurately and sensitively perceived through this technology, so it has broad application prospects in such fields as inertial navigation, mechanical vibration, dynamical control and medical care. Currently, researches on six-axis accelerometers remain in the exploratory stage. The main bottlenecks are the large amount of input and output information, as well as the overcoupled nonlinear vibration differential equations of the system, which make it difficult to decouple the six acceleration components timely, accurately and stably [1-10]. The proposed approaches which can achieve the six-dimensional acceleration sensing can

be divided into two categories: the combined measurement based on multiple uniaxial accelerometers (at least six) [1-4] and the measurement based on the single inertial mass-spring-damper system [5-10]. Wang et al. [1], proposed a coplanar layout principle of six uniaxial accelerometers to sense and measure the six-axis acceleration of a moving body. However, they obtained a closed-form solution of six-axis acceleration through accessing and decoupling the outputs from the six uniaxial accelerometers without considering the carrier's angular displacement and angular velocity relative to the reference system. Moreover, in the first category, individual accelerometers' misalignment and transverse sensitivity may severely affect the decoupling accuracy of the six acceleration components. Chapsky et al. [5], designed an isotropic six-axis accelerometer which uses six differential optical displacement sensors to detect the displacements of its single inertial mass supported by 24 elastic elements, where the six acceleration components can be calculated according to the output information from the six optical displacement sensors through a specially developed mathematical algorithm by ignoring the relative motion between the proof mass and carrier. Meng et al. [6], and Amarasinghe et al. [7], separately raised an elastic strain type six-axis accelerometer based on an E-type dual annular membranes structure and a quad-beam structure, by which the six acceleration components can be decoupled directly, but are limited to low-frequency and small-range measurement.

With the in-depth research on parallel mechanism theory, literature [9] and [10] studied the 6-SPS and 9-SPS parallel type six-axis accelerometers, respectively, where the 6-DOF parallel mechanism acts as the elastic body. However, due to its coupling configurations and sophisticating dynamics algorithms, the real-time decoupling characteristic of the six acceleration components is tremendously weakened. As to these difficulties, the technical improvements in parallel type six-axis accelerometers have taken two directions. The first involves neglecting the relative motions between the seismic-mass and the lower platform or linearizing the inverse kinematics solution to obtain an approximate solution of forward kinematics [8] to improve the calculation efficiency. It can obtain a result acceptable in a certain vibration amplitude and frequency range.

Another essential new design for this parallel type six-axis accelerometer involves structure decoupling that is the application of some special configurations with a closed-form solution of the forward kinematics to reduce the time consumption on the kinematics algorithm. This is the content studied in Sec. 2, including four configurations and a dynamics decoupling algorithm corresponding to 6, 7, 8 and 9 limbs parallel structure, separately. In addition, some researchers have investigated the different effects on the complexity, accuracy, stability, reliability and error in decoupling the six-axis acceleration when using a different number of uniaxial accelerometers and different allocation modes to construct a six-axis accelerometer [3-4]. Similarly, the studied four configurations are different in coupling degree, symmetry degree, spatial distribution and stiffness, etc. Therefore, from the point of mechanism design, a quantitative comparison of the different sensing characteristics between the studied four parallel type six-axis accelerometers is necessary to reveal the influential factors in realizing the six-axis acceleration sensing, as well as to determine the best application occasions of the different configurations. This is the content that the Sec. 3 focuses on.

2. Decoupling Algorithm

2.1 Six-axis acceleration sensing principle

This study belongs to the second category method to achieve the six-dimensional acceleration sensing, where the 6-DOF parallel mechanisms work as the elastic bodies, the piezoelectric ceramics act as the sensitive elements and play the role of prismatic pairs on

each limb. In the studied four configurations of parallel type six-axis accelerometer, the most representative one is the 6-UPS configuration whose simplified 3D model is shown in Fig. 1.
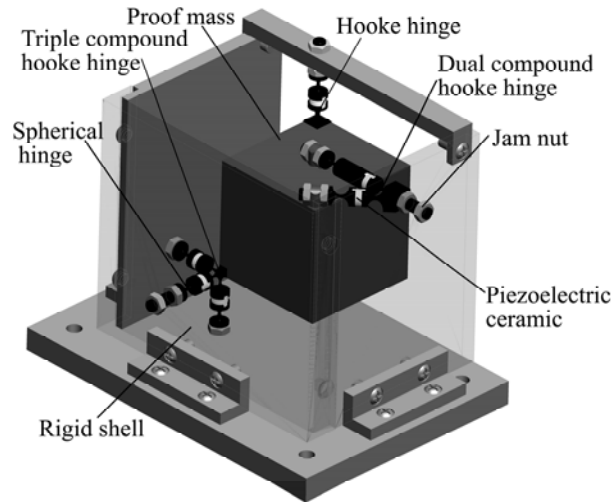
Fig. 1 The simplified 3D model of the 6-UPS six-axis accelerometer

The structural sketches of the studied four configurations are shown in Fig. 2 and Fig. 3, respectively. Similar to the 6-UPS physical prototype shown in Fig. 1, the cubic proof mass is connected to the rigid shell by n (n=6, 7, 8, 9, depending on the configuration itself) limbs, where each limb is composed of a flexible hooke hinge (abbreviated as U, denoted by "□" in Fig. 2 and Fig. 3), a prismatic pair (P, replaced by a piezo ceramic), and a flexible spherical hinge (S, denoted by "○"). If a parallel type six-axis accelerometer is mounted on a carrier with a six-axis accelerated motion, as to the accelerometer itself, there would produce two kinds of relative motions, including the relative motion between the proof mass and reference system, and the relative motion between the rigid shell and reference system, where the latter, which is used to characterize the motion state of the carrier, is the subject studied in this paper. In this sensing system, the six-axis acceleration of the carrier acts as the measured input signal, which is decoupled from the space movement of the proof mass.

When the six-axis accelerometer accelerates with the carrier, according to the d'Alembert principle, the n limbs have to provide equivalent active forces to balance the inertial forces of the proof mass. Thereby, the piezoelectric ceramics would produce expansion deformations along the axial direction after being forced. Due to the direct piezoelectric effect, a certain amount of charges would be generated but very weak in its direction of polarization, which should be sampled and converted to the voltage signals of low output impedance by the use of charge amplifier, and then collected by data acquisition equipment as the outputs at this instant. Afterwards, the carrier's six-axis acceleration, namely the measured input signals, can be obtained from those acquired data through a series of relevant decoupling algorithms derived in Sec. 2.2 and 2.3, where the algorithms in Sec.2.2 are used to represent the kinematics of the first relative motion based on the parallel mechanism and vector algebra, the algorithms in Sec. 2.3 just study the dynamics of the first relative motion based on Kane's dynamics and decoupling method of the six-axis acceleration of the second relative motion from the dynamical equations of the first one.

2.2 Kinematics Analysis

2.2.1 6-UPS configuration relative motion analysis

Here, take the most representative 6-UPS configuration whose simplified model is shown in Fig. 2 as an example to elaborate the direct kinematics of the proof mass relative to

the rigid shell. According to the voltage signals acquired by the data acquisition equipment, the length of individual limbs, l_i ($i=1, \ldots, 6$), can be reversibly and linearly calculated through the direct piezoelectric effect of piezoelectric ceramics and Hooke's Law [9]. In this design, the hinge points B_4, B_5 and B_6 are placed at the top surface diagonal of the cubic proof mass successively, whereas, if the lengths of the limbs A_4B_4 and A_4B_5, l_4 and l_5, are given, the length of virtual branch A_4B_6, l_7, will be known through the plane geometry. The deformation characteristics of all limbs in axial direction, including velocity $\dot{l}_i$ and acceleration $\ddot{l}_i$, are calculated by the use of the central difference formulas of order $o(h^2)$.
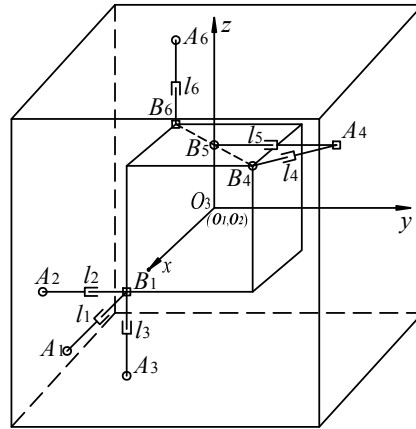

Fig. 2 The structural sketch of the 6-UPS six-axis accelerometer

Three Cartesian coordinate systems {M}, {S} and {I} are separately established on the proof mass, rigid shell and reference body, whose axes orientations are parallel to the cubic mass's three orthogonal edges and origins (O_1, O_2, O_3) coincide at the proof mass centroid initially. Based on the geometric properties of the tetrahedron, the spatial coordinate, velocity and acceleration analytical solutions of the hinge points B_1, B_4 and B_6 on the proof mass can be obtained in the tetrahedrons B_1-$A_1A_2A_3$, B_6-$B_1A_4A_6$ and B_4-$B_1B_6A_4$ relative to {S}, successively [11]. Thus, the position vector and rotation matrix describing the mass coordinate system {M} relative to the shell coordinate system {S} are given by

$$\begin{matrix}S\\M\end{matrix} \boldsymbol{p} = \frac{1}{3}\left({}^S\boldsymbol{r}_{O_2B_1} + {}^S\boldsymbol{r}_{O_2B_4} + {}^S\boldsymbol{r}_{O_2B_6} \right) + \frac{{}^S\boldsymbol{r}_{B_1B_6} \times {}^S\boldsymbol{r}_{B_1B_4}}{12a} \tag{1}$$

$$\begin{matrix}S\\M\end{matrix} \boldsymbol{R} = \boldsymbol{W}\boldsymbol{U}^{-1} \tag{2}$$

where $\boldsymbol{W} = [{}^S\boldsymbol{r}_{O_2B_1} - {}_M^S\boldsymbol{p}, {}^S\boldsymbol{r}_{O_2B_4} - {}_M^S\boldsymbol{p}, {}^S\boldsymbol{r}_{O_2B_6} - {}_M^S\boldsymbol{p}]$, $\boldsymbol{U} = [{}^M\boldsymbol{r}_{O_1B_1}, {}^M\boldsymbol{r}_{O_1B_4}, {}^M\boldsymbol{r}_{O_1B_6}]$, $2a$ is the cubic-mass's edge length, and a representation such as ${}_C^D\boldsymbol{E}$ in this study gives a description of vector/matrix $\boldsymbol{E}$ from coordinate system {C} to the reference system {D}, while the representation $\boldsymbol{r}_{AB}$ means the vector from the point A to B.

Respectively, the angular velocity, angular acceleration, linear velocity and linear acceleration vectors of the proof mass relative to the shell coordinate system {S} are given by

$$\begin{matrix}S\\M\end{matrix} \hat{\boldsymbol{\omega}} = {}_M^S\dot{\boldsymbol{R}} {}_M^S\boldsymbol{R}^T \tag{3}$$

$$\begin{matrix}S\\M\end{matrix} \hat{\boldsymbol{a}} = {}_M^S\ddot{\boldsymbol{R}} {}_M^S\boldsymbol{R}^T + {}_M^S\dot{\boldsymbol{R}} {}_M^S\dot{\boldsymbol{R}}^T \tag{4}$$

$$\begin{matrix}S\\M\end{matrix} \boldsymbol{V} = {}^S\boldsymbol{V}_{B1} + {}_M^S\boldsymbol{\omega} \times {}^S\boldsymbol{r}_{B1O1} \tag{5}$$

$$\begin{matrix}S\\M\end{matrix} \boldsymbol{a} = {}^S\boldsymbol{a}_{B1} + {}_M^S\boldsymbol{\alpha} \times {}^S\boldsymbol{r}_{B1O1} + {}_M^S\boldsymbol{\omega} \times ({}_M^S\boldsymbol{\omega} \times {}^S\boldsymbol{r}_{B1O1}) \tag{6}$$

where the forms like $\hat{\boldsymbol{q}}$, $\dot{\boldsymbol{q}}$ and $\ddot{\boldsymbol{q}}$ represent the skew-symmetric matrix, the first-order and second-order time derivatives corresponding to the vector or matrix $\boldsymbol{q}$, respectively, $^{S}V_{B1}$ and $^{S}\boldsymbol{a}_{B1}$ indicate the velocity and acceleration vector of the hinge point B_1, respectively.

2.2.2   Other Configurations Analysis

The structural schematic representations of 7-UPS, 8-UPS and 9-UPS parallel type six-axis accelerometers are shown in Fig. 3.

(a) 7-UPS configuration   (b) 8-UPS configuration   (c) 9-UPS configuration
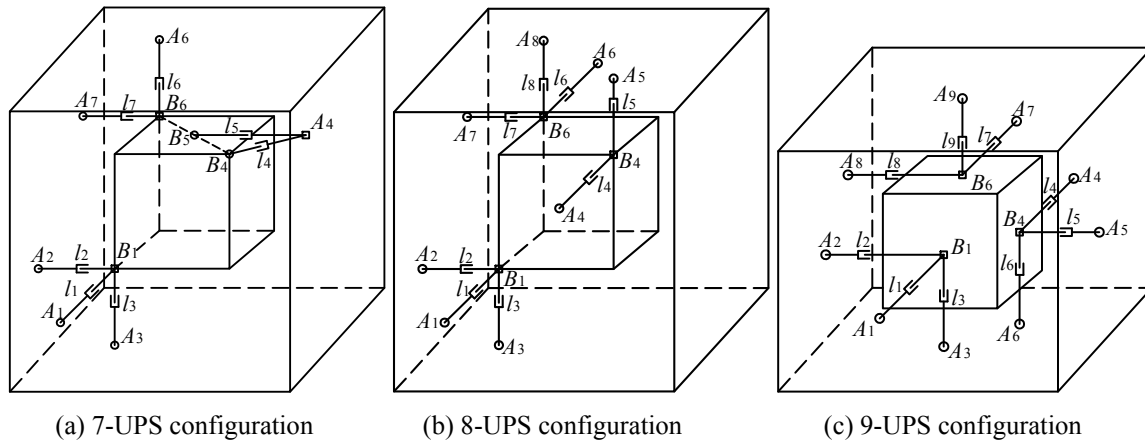
Fig. 3 The structural schematic representation of the three parallel type six-axis accelerometers

As shown in Fig. 3(a), the 7-UPS configuration is similar to the 6-UPS configuration except for the original flexible hooke hinge at B_6 which was replaced by a flexible dual compound hooke hinge, thus the motion characteristics of the hinge point B_6 can be obtained using tetrahedron theorem in B_6-$B_1A_6A_7$, as well as in B_6-$B_1A_4A_6$. Although this configuration has a closed-form solution of the forward kinematics, due to the inherent properties of the data acquisition, the limbs' compression and tension deformation characteristics in axial direction can only be calculated using the numerical differentiation methods. As a result, the involved velocity and acceleration errors of the hinge point B_1 would be transferred to B_6. Given the error factors from data acquisition, signal processing, model machining and assembling, etc. in actual working conditions, the kinematics of the hinge point B6 are obtained by the two methods mentioned above, which would undoubtedly produce two slightly different results. Afterwards, their respective weights can be determined by a large number of computer simulations and experiments, so it becomes possible to find a more precise kinematic solution through the interpolation method, which will contribute to the compensation of the kinematic errors, as well as the improvement in measurement accuracy. In addition, this paper aims at studying the influences of the configurations on the performance of several parallel type six-axis accelerometers theoretically. Thus, the experimental aspects will be further studied in another paper.

As the 8-UPS configuration shown in Fig. 3(b), a flexible triple compound hooke hinge and a flexible dual compound hooke hinge are mounted on the hinge points B_6 and B_4 on the proof mass, respectively. Consequently, the kinetic characteristics of B_1 and B_6 can be calculated in the tetrahedron B_1-$A_1A_2A_3$ and B_6-$A_6A_7A_8$ independently, which would enhance the decoupling efficiency of the six-axis acceleration components. Moreover, according to the invariant length B_1B_6 and the theorem of projection of velocity/acceleration along B_1B_6, a series of constraint stabilization should be made to compensate the errors from numerical differentiation or other data handling procedures and inhibit the accumulation of errors.

As the 9-UPS configuration shown in Fig. 3(c), fix three triple compound hooke hinges at the hinge points B_1, B_4 and B_6 which are located at the center of three mutually perpendicular planes of the cubic mass, successively. The motion characteristics of the three hinge points B_1, B_4 and B_6 can be obtained in the tetrahedron B_1-$A_1A_2A_3$, B_4-$A_4A_5A_6$ and B_6-$A_7A_8A_9$, respectively, thus, the computational efficiency in kinematics is tremendously improved [10]. Also, a violated correction should be made as the way employed in 8-UPS configuration to restrain the cumulative errors from the numerical methods.

The above mentioned three configurations of six-axis accelerometer have an analogous kinematics algorithm as the 6-UPS configuration's analyzed in Sec. 2.2.1. As space is limited, no detailed modelling process is given.

2.2.3   Absolute motion analysis

As to the relative motion between the rigid shell and reference system, transform the rotation matrix ${}^I_S\boldsymbol{R}$ and angular velocity ${}^I_S\boldsymbol{\omega}$ to a homogeneous representation and denote them as Eqns. (8) and (9) using the unit quaternion $\boldsymbol{\xi}$ [12, 13].

$$\boldsymbol{\xi} = \begin{pmatrix} \varepsilon_1 & \varepsilon_2 & \varepsilon_3 & \varepsilon_4 \end{pmatrix}^T = \begin{pmatrix} \boldsymbol{\varepsilon}^T & \varepsilon_4 \end{pmatrix}^T \tag{7}$$

$$\,{}^I_S\tilde{\boldsymbol{R}} = \begin{pmatrix} {}^I_S\boldsymbol{R} & \boldsymbol{0} \\ \boldsymbol{0} & 1 \end{pmatrix} = \left(\overset{+}{\boldsymbol{\xi}}\right)\left(\overset{-}{\boldsymbol{\xi}}\right)^T = \left(\overset{-}{\boldsymbol{\xi}}\right)^T\left(\overset{+}{\boldsymbol{\xi}}\right) \tag{8}$$

$$\,{}^I_S\tilde{\boldsymbol{\omega}} = \begin{pmatrix} {}^I_S\boldsymbol{\omega} \\ 0 \end{pmatrix} = 2\left(\overset{-}{\boldsymbol{\xi}}\right)^T\left(\dot{\boldsymbol{\xi}}\right) \tag{9}$$

where $\left(\overset{+}{\boldsymbol{\xi}}\right) = \begin{pmatrix} \varepsilon_4\boldsymbol{E} + \hat{\boldsymbol{\varepsilon}} & \boldsymbol{\varepsilon} \\ -\boldsymbol{\varepsilon}^T & \varepsilon_4 \end{pmatrix}$, $\left(\overset{-}{\boldsymbol{\xi}}\right) = \begin{pmatrix} \varepsilon_4\boldsymbol{E} - \hat{\boldsymbol{\varepsilon}} & \boldsymbol{\varepsilon} \\ -\boldsymbol{\varepsilon}^T & \varepsilon_4 \end{pmatrix}$, $\left(\overset{+}{\boldsymbol{\xi}}\right)$ and $\left(\overset{-}{\boldsymbol{\xi}}\right)$ are orthogonal matrixes, $\boldsymbol{E}$ is the 3×3 identity matrix.

According to vector algebra, the absolute angular velocity and angular acceleration of {M} with respect to the inertial frame {I} are given by

$$\,{}^I_M\boldsymbol{\omega} = {}^I_S\boldsymbol{\omega} + {}^I_S\boldsymbol{R}\,{}^S_M\boldsymbol{\omega} \tag{10}$$

$$\,{}^I_M\boldsymbol{\alpha} = {}^S_M\dot{\boldsymbol{\omega}} = {}^I_S\boldsymbol{\alpha} + {}^I_S\boldsymbol{R}\,{}^S_M\boldsymbol{\alpha} + {}^I_S\boldsymbol{\omega} \times {}^I_S\boldsymbol{R}\,{}^S_M\boldsymbol{\omega} \tag{11}$$

Assume the position vector ${}^I_S\boldsymbol{p} = (p_x, p_y, p_z)^T$, the absolute position and linear acceleration vector of the centroid of cubic proof mass are calculated as followings

$$\,{}^I_M\boldsymbol{p} = {}^I_S\boldsymbol{R}\,{}^S_M\boldsymbol{p} + {}^I_S\boldsymbol{p} \tag{12}$$

$$\,{}^I_M\boldsymbol{a} = {}^I_M\ddot{\boldsymbol{p}} = 2\,{}^I_S\boldsymbol{\omega} \times {}^I_S\boldsymbol{R}\,{}^S_M\boldsymbol{V} + {}^I_S\boldsymbol{\omega} \times ({}^I_S\boldsymbol{\omega} \times {}^I_S\boldsymbol{R}\,{}^S_M\boldsymbol{p}) + {}^I_S\boldsymbol{\alpha} \times {}^I_S\boldsymbol{R}\,{}^S_M\boldsymbol{p} + {}^I_S\boldsymbol{R}\,{}^S_M\boldsymbol{a} + {}^I_S\boldsymbol{a} \tag{13}$$

where ${}^I_S\boldsymbol{a} = {}^I_S\ddot{\boldsymbol{p}}$, ${}^I_S\boldsymbol{\alpha} = {}^I_S\dot{\boldsymbol{\omega}}$ indicate the linear acceleration and angular acceleration of the rigid shell relative to the inertial frame {I}, respectively, which are the unknown six-axis acceleration used to characterize the motion state of the carrier and required to be decoupled out.

Here, the absolute motion of the proof mass, which is constructed by the relative motion between the proof mass and rigid shell (known, analyzed in Sec. 2.2.1) and the relative

motion between the rigid shell and reference system (unknown, analyzed in 2.2.3), has been obtained. All that requires is to establish a relation between the derived absolute acceleration of the proof mass and the output signals from the piezoelectric ceramics.

2.3 Dynamics Analysis

2.3.1 Kane's dynamical equations

This is a holonomic constraint system with 6 DOF, but only six of the seven generalized coordinates (ε_1, ε_2, ε_3, ε_4, p_x, p_y, p_z) are independent mutually, which requires an extra constraint equation to solve the dynamical formulae, and that increases the decoupling difficulties. Therefore, constitute six independent quasi-velocities u_s by a linear combination of the seven generalized velocities as Eqns. 14 [14-16].

$$u_s = u_s(\dot{\varepsilon}_1, \dot{\varepsilon}_2, \dot{\varepsilon}_3, \dot{\varepsilon}_4, \dot{p}_x, \dot{p}_y, \dot{p}_z; t), s = 1, 2, \cdots 6 \tag{14}$$

The absolute linear velocity and angular velocity of proof mass are written in the form:

$$_M^I \boldsymbol{\Gamma} = \begin{pmatrix} _M^I \boldsymbol{V} \\ _M^I \boldsymbol{\omega} \end{pmatrix} = \boldsymbol{v}\boldsymbol{u} \tag{15}$$

where $\boldsymbol{v} = \begin{pmatrix} \boldsymbol{V} \\ \boldsymbol{\omega} \end{pmatrix} = \begin{pmatrix} \boldsymbol{i} & \boldsymbol{j} & \boldsymbol{k} & \boldsymbol{0} & \boldsymbol{0} & \boldsymbol{0} \\ \boldsymbol{0} & \boldsymbol{0} & \boldsymbol{0} & \boldsymbol{i} & \boldsymbol{j} & \boldsymbol{k} \end{pmatrix}$,

$\boldsymbol{u} = \begin{pmatrix} _M^I V_x & _M^I V_y & _M^I V_z & _M^I \omega_x & _M^I \omega_y & _M^I \omega_z \end{pmatrix}^T$, select $\boldsymbol{u}$ as the quasi-velocities of the holonomic constraint system, while the linear coefficient matrix $\boldsymbol{v}$ can be regarded as the partial velocity matrix corresponding to $\boldsymbol{u}$.

Compared with the whole system, it is reasonable to neglect the influences from the mass, inertia moment and damping force of the piezoelectric ceramics on decoupling the six-axis acceleration. Assume the cubic proof mass as a rigid body, the active forces exerted on the proof mass are equivalent to a couple of force $^I \boldsymbol{R}_m$ together with a torque $^I \boldsymbol{L}_m$ that are

$$^I \boldsymbol{R}_m = \sum_{i=1}^{n} \frac{Q_i}{d_{33}} {}^I \boldsymbol{e}_i + M {}^I \boldsymbol{g} \tag{16}$$

$$^I \boldsymbol{L}_m = \sum_{i=1}^{n} \frac{Q_i}{d_{33}} \left({}^I \boldsymbol{r}_i \times {}^I \boldsymbol{e}_i \right) \tag{17}$$

where

n is equal to the number of limbs of the selected configuration, n=6, 7, 8, 9,

Q_i indicates the quantity of electric charge generated by the piezoelectric ceramic mounted on the ith limb,

d_{33} is the piezoelectric modulus at the polarization direction of piezoelectric ceramics,

$^I \boldsymbol{e}_i$ indicates the direction vector of the ith limb,

M is the proof mass,

$^I \boldsymbol{g}$ is the gravitational acceleration measured by gravity gradiometer,

$^I \boldsymbol{r}_i$ is the vector from the mass centre to its hinge point on the ith limb.

The corresponding generalized active forces are given by

$$K = v^T \begin{pmatrix} ^I\!R_m \\ ^I\!L_m \end{pmatrix} \tag{18}$$

Similarly, the inertia forces principal vector $^I\!R_m^*$, principal moment $^I\!L_m^*$ and the generalized inertia forces K^* exerted on the proof mass are given by

$$^I\!R_m^* = -M \, {}_M^I a \tag{19}$$

$$^I\!L_m^* = -{}_M^I J \, {}_M^I \alpha - {}_M^I \omega \times {}_M^I J \, {}_M^I \omega \tag{20}$$

$$K^* = v^T \begin{pmatrix} ^I\!R_m^* \\ ^I\!L_m^* \end{pmatrix} \tag{21}$$

where $_M^I J$ indicates the inertia tensor matrix of the proof mass relative to inertial frame $\{I\}$, obtained by using the axial screw transform formula as Eqn. 22.

$$_M^I J = {}_S^I R \, {}_M^S R \, {}^M J \, {}_M^S R^T \, {}_S^I R^T \tag{22}$$

Hence, all that remains to be done is to substitute from Eqns. 18 and 21 into Kane's dynamical equations (Eqns. 23), namely,

$$K + K^* = 0 \tag{23}$$

Thus, the six strong coupling dynamical scalar equations are obtained, which cannot be solved separately.

2.3.2 Decoupling method

At this point, the relationship between the inputs and outputs of this sensor system has been established in dynamical equations 23, all that remains is how to decouple out the linear acceleration $_S^I a$ and angular acceleration $_S^I \alpha$ from it. The three scalar equations only related to the angular acceleration in Eqns. 23 can be simplified as

$$^I\!L_m - {}_M^I J \left({}_S^I \alpha + {}_S^I R \, {}_M^S \alpha + {}_S^I \omega \times {}_S^I R \, {}_M^S \omega \right) - \left({}_S^I \omega + {}_S^I R \, {}_M^S \omega \right) \times {}_M^I J \cdot \left({}_S^I \omega + {}_S^I R \, {}_M^S \omega \right) = 0 \tag{24}$$

where Eqns. 24 are a set of strongly coupled second-order nonlinear differential equations actually, including $\varepsilon_1, \varepsilon_2, \varepsilon_3, \varepsilon_4, \dot{\varepsilon}_1, \dot{\varepsilon}_2, \dot{\varepsilon}_3, \dot{\varepsilon}_4, \ddot{\varepsilon}_1, \ddot{\varepsilon}_2, \ddot{\varepsilon}_3, \ddot{\varepsilon}_4$, which are still very difficult to be solved directly utilizing the analytical method or numerical method.

Hence, we introduce an auxiliary angular velocity $^S\omega$ meeting the relation

$$_S^I \omega = {}_S^I R \, {}^S \omega \tag{25}$$

where the physical meaning of $^S\omega$ is the projection of angular velocity $_S^I \omega$ in the coordinate system $\{S\}$.

Substitution from Eqn. 25 into Eqns. 24 and simplification leads to

$$\begin{cases} {}^{S}\dot{\boldsymbol{\omega}} = {}^{S}\boldsymbol{J}^{-1}\,{}^{S}_{M}\boldsymbol{L}_m - {}^{S}_{M}\boldsymbol{\alpha} - {}^{S}\boldsymbol{\omega}\times{}^{S}_{M}\boldsymbol{\omega} - {}^{S}\boldsymbol{J}^{-1}\left(\left({}^{S}\boldsymbol{\omega}+{}^{S}_{M}\boldsymbol{\omega}\right)\times{}^{S}\boldsymbol{J}\cdot\left({}^{S}\boldsymbol{\omega}+{}^{S}_{M}\boldsymbol{\omega}\right)\right) \\ {}^{S}\boldsymbol{J} = {}^{S}_{M}\boldsymbol{R}^{M}\boldsymbol{J}\,{}^{S}_{M}\boldsymbol{R}^{T} \end{cases} \tag{26}$$

Thus, the second-order nonlinear differential equations, Eqns. 24, including ${}^{S}\boldsymbol{\omega}$ and ${}^{S}\dot{\boldsymbol{\omega}}$, are converted to the first-order unsteady linear ones, Eqns. 26. After calibrating the six-axis accelerometers at the initial time, it does not obscure to obtain ${}^{S}\boldsymbol{\omega}$ and ${}^{S}\dot{\boldsymbol{\omega}}$ timely using the improved Euler Algorithm as the Eqns. 27.

$$\begin{cases} {}^{S}\overline{\boldsymbol{\omega}}_{i+1} = {}^{S}\boldsymbol{\omega}_i + h\,{}^{S}\dot{\boldsymbol{\omega}}_i\big|_{(t_i,\,{}^{S}\boldsymbol{\omega}_i)} \\ {}^{S}\boldsymbol{\omega}_{i+1} = {}^{S}\boldsymbol{\omega}_i + \dfrac{h}{2}[{}^{S}\dot{\boldsymbol{\omega}}_i\big|_{(t_i,\,{}^{S}\boldsymbol{\omega}_i)} + {}^{S}\dot{\boldsymbol{\omega}}_i\big|_{(t_{i+1},\,{}^{S}\overline{\boldsymbol{\omega}}_{i+1})}] \end{cases} \tag{27}$$

where i denotes the ith sampling step, h is the step size, t_i indicates the sampling time of the ith step, ${}^{S}\overline{\boldsymbol{\omega}}_{i+1}$ and ${}^{S}\boldsymbol{\omega}_{i+1}$ denote the predictor and corrector of ${}^{S}\boldsymbol{\omega}$ at t_{i+1}, respectively.

Specifically, the simultaneous Eqns. 8, 9 and 25 yield

$$\left(\dot{\boldsymbol{\xi}}\right) = \frac{1}{2}\begin{pmatrix} + \\ \boldsymbol{\xi} \end{pmatrix}\begin{pmatrix} {}^{S}\boldsymbol{\omega} \\ 0 \end{pmatrix} \tag{28}$$

Similarly, the quaternion parameter $\boldsymbol{\xi}$ and its derivative $\dot{\boldsymbol{\xi}}$ can be obtained timely from Eqn. 28 through the improved Euler Algorithm, which need to be corrected by the constraint stabilization to eliminate the cumulative errors from the numerical calculations. Referring to Eqns. 8, 9 and 24, the rotation matrix ${}^{I}_{S}\boldsymbol{R}$, angular velocity ${}^{I}_{S}\boldsymbol{\omega}$ and angular acceleration ${}^{I}_{S}\boldsymbol{\alpha}$ of the six-axis accelerometer relative to the inertial frame $\{I\}$ can be obtained with the data acquisition, successively and synchronously (Here, only the decoupling algorithm is discussed without considering the time consumption in data transmission, signal processing, etc.).

Synthesizing the kinematics analysis in Sec. 2.2, and substituting ${}^{I}_{S}\boldsymbol{R}$, ${}^{I}_{S}\boldsymbol{\omega}$ and ${}^{I}_{S}\boldsymbol{\alpha}$ into the rest three Kane's dynamical equations (Eqns. 23), the linear acceleration vector ${}^{I}_{S}\boldsymbol{a}$ is got, which is the unknown linear acceleration of the carrier relative to the inertial frame $\{I\}$. Now, the carrier's six-axis acceleration is obtained by numerical methods as Eqn. 29.

$$A = [\,{}^{I}_{S}\boldsymbol{a}^{T} \quad {}^{I}_{S}\boldsymbol{\alpha}^{T}\,]^{T} \tag{29}$$

3. Static characteristics comparison

There are several static characteristic indices of the six-axis accelerometer, but only a proper and scientific analysis of the indices that are directly affected by the configurations can guide the mechanism design more effectively. So, our research was conducted on accuracy, efficiency, sensitivity, isotropy, and working frequency bandwidth of the mentioned four parallel type six-axis accelerometers to find out those influential factors.

According to the four parallel type six-axis accelerometers mentioned in Sec.2, we establish four virtual prototypes in the Automatic Dynamic Analysis of Mechanical Systems (ADAMS), where the relative geometric parameters are set as a=22.5mm, l=23.0mm, m=0.710866kg. Therein, the 6-UPS prototype is shown in Fig. 4.
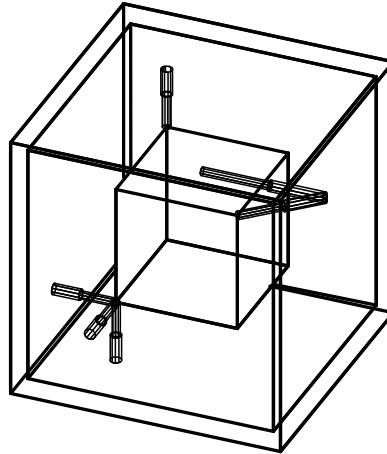
Fig. 4 The 6-UPS virtual prototype in ADAMS

Afterwards, impose a linear drive and a rotation drive with the displacement drive functions $\kappa=6.34\cos(\omega t)-6.34$(mm) and $\varphi=5.00\cos(\omega t)-5.00$(deg) on the rigid shell along the direction of (14, -15, 16) and (-9, -12, 7), respectively, to create a virtual vibration environment with a six-dimensional acceleration. Successively, collect the axial deformation of the n limbs in the four virtual prototypes within a simulation time of 2s, the collected data can be regarded as the transformed output signals from piezoelectric ceramics. The six-axis acceleration of the carrier, denoted by A_S, can be found as the indication of the six-axis accelerometer according to the kinematics and dynamics algorithms in Sec. 2; while the imposed six-axis acceleration on the virtual prototype can be regarded as the conventional true value, denoted by A_r. Introducing the fiducial error to indicate the decoupling principle accuracy, which makes the linear and angular acceleration errors more intuitive and comparable. The fiducial error matrix is given by

$$A_q = G^{-1}(A_s - A_r) \tag{30}$$

where $A_q = [\gamma_1, \gamma_2, \gamma_3, \gamma_4, \gamma_5, \gamma_6]^T$, whose elements are the fiducial errors of the linear acceleration along the direction of x, y and z of the inertial frame $\{I\}$, and then the angular acceleration's, successively; G is a diagonal matrix whose leading diagonal elements are the full range of the linear acceleration along the direction of x, y and z, and the angular acceleration's, successively.

To be clear, when deriving the decoupling algorithms of the first category six-axis accelerometer, Wang et al. [1] ignored the angular displacement and angular velocity of the carrier to find an analytical solution, which limits their algorithms so that they can only be used in micro-amplitude and low-frequency vibration occasions. However, referring to Eqns. 25 and 26, the structure of the dynamical equations derived in Sec. 2 is independent of the angular movement of the carrier, so that the algorithms have a universal adaptability and the angular motion amplitude can be freely selected. Here, the angular motion amplitude is selected as 5 degrees.

3.1 Accuracy Comparison

Considering that the carrier's vibration frequency and time step size (Eqn. 27) may have a definite impact on the principle accuracy (also calculation accuracy) of the studied four parallel type six-axis accelerometers, without loss of generality, this impact is corroborated through computer simulations by the controlling variable method in ADAMS with a vibration frequency ranging from 2.0Hz to 26.0Hz and a time step size from 10^{-5}s to 10^{-2}s separately.

Based on the algorithms of kinematics and dynamics derived in Sec. 2, we can create MATLAB programs to calculate the six acceleration components. In this research, the comprehensive accuracy of the six-axis accelerometers is measured by the maximum fiducial error and global fiducial error which are given by Eqns. 31 and 32, separately, where the former is used to determine the accuracy classes, and the latter to measure the error divergence characteristics. The larger the error value, the lower the calculation accuracy. The principle accuracy indices are depicted in Fig. 5 and Fig. 6, respectively, where the former aims to study the influences of vibration frequency on the principle accuracy (the time step size is set as 10^{-3}s), and the latter to describe the influences of time step size on it (the vibration frequency is 10Hz). Therefore, given the influences of the two aspects on the result, in order to make Fig. 5 and Fig. 6 more self-evident, the adimensional parameter "vibration frequency (f) × step size (h) τ" is taken as abscissa.

$$\delta_{1(3)} = \frac{1}{6} \sum_{i=1}^{6} |\gamma_i|_{max} \tag{31}$$

$$\delta_{2(4)} = \frac{1}{6} \sum_{i=1}^{6} \left| \int_{t_0}^{t_1} \gamma_i \, dt \right| \tag{32}$$
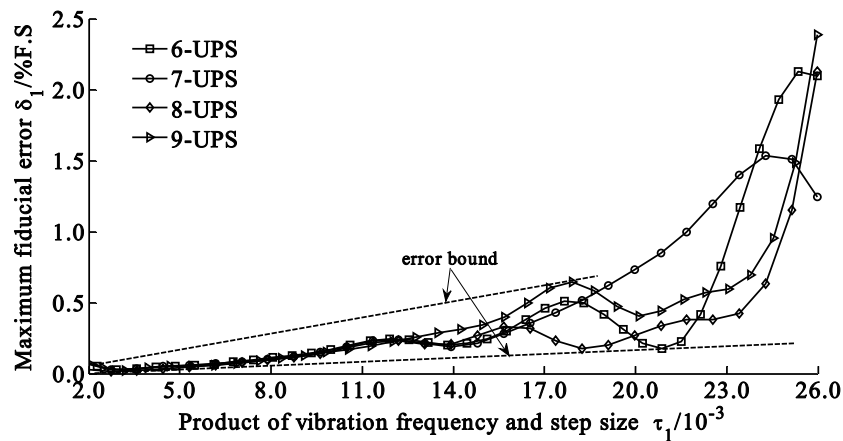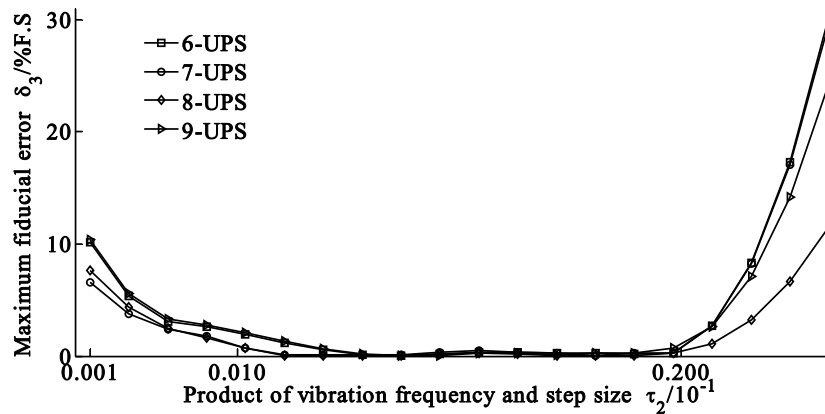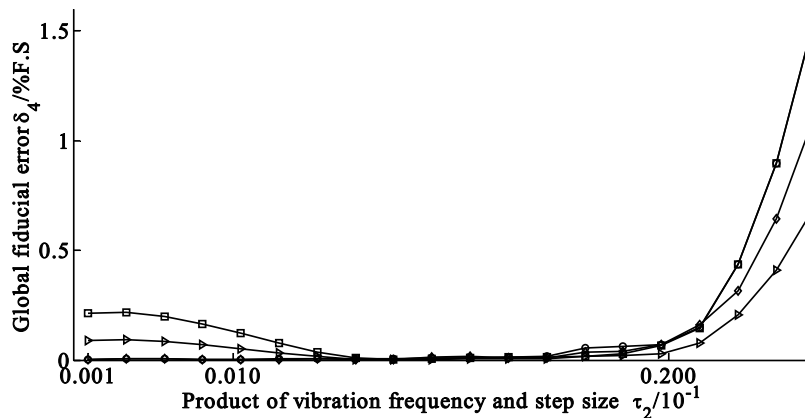

(a) Maximum fiducial error
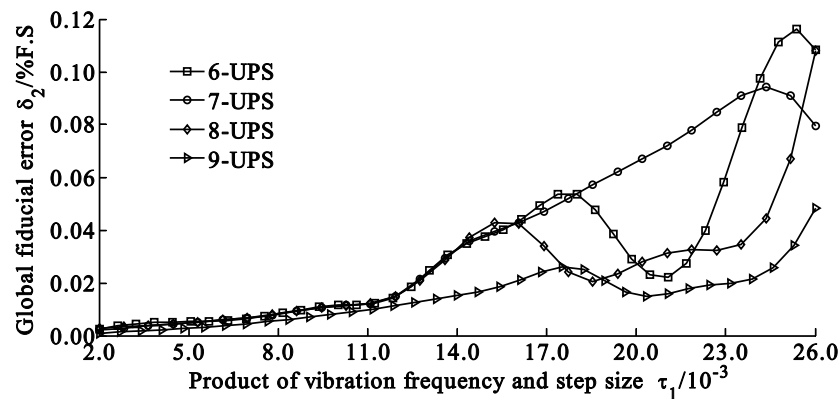
(b) Global fiducial error

Fig. 5 The relation between principle accuracy and vibration frequency of the four six-axis accelerometers

(a) Maximum fiducial error

(b) Global fiducial error

Fig. 6 The relation between principle accuracy and step size of the four six-axis accelerometers

The plots in Figs. 5 and 6 imply that:

(1) Referring to Fig. 5, the error magnitude of the four six-axis accelerometers obtained through the same decoupling algorithm almost keep equivalent with an error growth-rate of approximately $0.024\%F.S/10^{-3}$ and a narrow error bound in low vibration frequency, which effectively validates the correctness of the derived decoupling algorithm in Sec. 2 and also reveals one of the inherent properties of the parallel type six-axis accelerometer that the output from each piezoelectric ceramic is regarded as the useful information to participate in the calculation of the six acceleration components.

(2) The time step size "h" plays the role of the regularization parameter in the decoupling algorithm derived in Sec. 2, neither too big nor too small is appropriate. Referring to Fig. 6, if the step size "h" is greater than 2×10^{-3}s, the 8-UPS configuration can guarantee a more precise decoupling result. And if "h" is selected ranging from 10^{-4}s to 2×10^{-3}s, the maximum fiducial error and global fiducial error of the four six-axis accelerometers remain less than $2.01\%F.S$ and $0.12\%F.S$, respectively, meanwhile, there is no obvious diversity between the four parallel type six-axis accelerometers. At last, if "h" is less than 10^{-4}s, the errors become larger because of the increases in numerical differential errors and integration times, which also sacrifices the decoupling efficiency.

(3) It is a common drawback of all inertia sensors that the error diverges over time in measurement. In spite of the same error magnitude of the four parallel type six-axis accelerometers, their error divergence modes are different from each other. Hence, the time-

integration of the fiducial error, namely, the velocity fiducial error, can efficiently and globally reveal the divergent characteristics of the decoupled acceleration errors. The plots in Fig. 5 (b) and Fig. 6 (b) show that the 9-UPS configuration has the best accuracy stability in a short time and an extensive step size range.

(4) The principle accuracy of the four accelerometers decreases with the increase in carrier's vibration frequency. After further analysis, we found that the jerk of the proof mass gradually increases with the increase in vibration frequency, so that each limb suffers a larger axial force and length change rate, making the numerical differential errors in getting the limbs' axial deformation characteristics larger. In addition, those errors are accumulated over time in solving the dynamics Eqns. 23 by the use of the improved Euler algorithm, resulting in a reduction of the overall principle accuracy. The performed simulations have verified that increasing the frequency of data acquisition appropriately (referring to Fig. 6 (b)) or improving decoupling algorithm can improve this trend, but both reduce the calculating efficiency [10].

3.2   Efficiency Comparison

Investigating the decoupling arithmetic processes corresponding to the four different configurations both in kinematics and dynamics, Sec. 2.2 and 2.3, the amount of computation differs from each other in obtaining a set of carrier's six-axis acceleration by the use of the same decoupling algorithm, as shown in Table 1. As a result, the computational efficiency is different from each other [17].

Table 1 Assessment of computational efficiency of the four six-axis accelerometers

Configurations		6-UPS	7-UPS	8-UPS	9-UPS
Obtain a set of six-axis acceleration	Processed data	18	21	24	27
	Multiplications	2830	2767	2482	2028
	Additions	1173	1162	997	804
Time consumption in dealing with the collected data in 2s t/s		1.967	1.972	1.635	1.225
Max allowable acquisition frequency f/Hz		1016.8	1014.2	1223.2	1632.7

Note:
The relevant data in Table 1 was assessed based on the Matlab 6.5 and a computer with the configurations of Intel(R) Core(TM) i3-2120 CPU @3.30GHz and 6.00GB of RAM.

Combined with the analysis in Sec. 2.2 and 2.3, Table 1 indicates that:

(1) Aiming at the four accelerometers with different configurations, the coupling complexities in both kinematics and dynamics decrease while the limbs increase, which reduces the amount of computation. In particular, the 9-UPS configuration has the least calculation amount which leads to the most efficient computation.

(2) Compared with the 6-UPS configuration, the algorithm itself of the 7-UPS configuration is slightly less time-consuming, but it needs to read three more groups of data to decouple out a set of six-axis acceleration, which leads to the total data processing time a little longer, namely, a lower computational efficiency.

(3) For the four six-axis accelerometers, the maximum frequencies of data acquisition that can guarantee the real-time decoupling are obtained. According to the Nyquist-Shannon sampling theorem, if the carrier's vibration frequency is less than 508Hz, all four six-axis

accelerometers can fulfil the real-time decoupling requirement, while exceeding 816Hz, the decoupling algorithm needs to be modified to improve computational efficiency.

3.3 Sensitivity Comparison

The sensitivity of the parallel type six-axis accelerometer is referred to as the axial strain of each elastic element generated under the action of unit acceleration. In this research, the absolute value of the output signal from the piezoelectric ceramic which makes the greatest contribution to generate a unit uniaxial acceleration is defined as the sensitivity along this axis. Excluding the influences caused by gravity in consequence of its unsteady effects in determining the angular acceleration sensitivity, impose the unit linear acceleration (1g) and the unit angular acceleration (1rad/s^2) on the established four virtual prototypes of six-axis accelerometers along the directions of x, y and z relative to the inertial frame $\{I\}$ successively, and then acquire the axial deformation of the n (n=6, 7, 8, 9) limbs when the proof mass arrives at a stable state relative to the rigid shell. The collected data are transformed to the electric charges based on the direct piezoelectric effect, where the piezoelectric constant (d_{33}) and the elastic compliance (S_{33}^{E}) are set as 400pc/N and 1.90×10^{-11}m^2/N according to the P-51 series PZT, respectively. Combined with the kinematics analysis in Sec. 2.2, the sensitivity is given by

$$S = \begin{pmatrix} S_a \\ S_\alpha \end{pmatrix} = \left(\frac{\left| Q_{ai} e_i \cdot i \right|_{max}}{\left| e_i \cdot i \right|} \quad \frac{\left| Q_{aj} e_j \cdot j \right|_{max}}{\left| e_j \cdot j \right|} \quad \frac{\left| Q_{ak} e_k \cdot k \right|_{max}}{\left| e_k \cdot k \right|} \quad \frac{\left| Q_{\alpha i} r_i \times e_i \cdot i \right|_{max}}{\left| r_i \times e_i \cdot i \right|} \right.$$
$$\left. \frac{\left| Q_{\alpha j} r_j \times e_j \cdot j \right|_{max}}{\left| r_j \times e_j \cdot j \right|} \quad \frac{\left| Q_{\alpha k} r_k \times e_k \cdot k \right|_{max}}{\left| r_k \times e_k \cdot k \right|} \right)^T , \quad i, j, k = 1, 2, 3, 4, 5, 6 \tag{33}$$

where the vectors are all represented in the shell frame $\{S\}$ whose direction vectors are i, j and k; $S_a(S_{ax}, S_{ay}, S_{az})$ is the linear acceleration sensitivity vector whose elements are the three sensitivity components of linear acceleration along the direction of i, j and k successively, while $S_\alpha(S_{\alpha x}, S_{\alpha y}, S_{\alpha z})$ corresponds to the angular acceleration sensitivity. Q_{ai}, Q_{aj}, Q_{ak}, $Q_{\alpha i}$, $Q_{\alpha j}$ and $Q_{\alpha k}$ indicate the collected electric charges generated by the piezoelectric ceramics under an action of unit linear acceleration and unit angular acceleration along the directions of i, j and k successively. The linear and angular acceleration synthetic sensitivity are given by Eqns. 34 separately.

$$\begin{cases} S_a = \left(S_{ax} + S_{ay} + S_{az} \right) / 3 \\ S_\alpha = \left(S_{\alpha x} + S_{\alpha y} + S_{\alpha z} \right) / 3 \end{cases} \tag{34}$$

The sensitivity comparison between the four six-axis accelerometers is shown in Table 2.

Table 2 Sensitivity comparison between the four six-axis accelerometers

Configurations	6-UPS	7-UPS	8-UPS	9-UPS
Linear acceleration sensitivity S_a /nc/g	4.451	4.157	3.098	3.873
Angular acceleration sensitivity S_α/pc/rad/s^2	5.933	5.082	3.258	5.332

The observation and analysis of Table 2 show that:

(1) The 6-UPS configuration has the most superior sensitivity. As to the 6-UPS configuration, the least limbs cause the weakest stiffness, so that the spatial vibration amplitude of the proof mass, including translation and rotation, would be larger under the action of the same acceleration, so do the strains of the piezoelectric ceramics.

(2) Both the linear acceleration and angular acceleration sensitivities take a reduction from the 6-UPS to 8-UPS configuration. The key reason is the increase in structural stiffness which is strengthened by the redundant limbs. But the 9-UPS configuration seems to violate this principle, which is caused by the redistribution of the compound hinges. Thus, the sensitivity of the six-axis accelerometer is affected by the allocation modes of the n limbs in some extent.

3.4 Isotropy comparison

3.4.1 Sensitivity Isotropy

Sensitivity isotropy [8], including the linear acceleration sensitivity isotropy and angular acceleration isotropy, are judged by the ratio of the minimum sensitivity to the maximum one of the three linear and angular acceleration components which are given by Eqns. 35. This index just reflects the sensitivity characteristics in all directions in theory; the sensitivity isotropy of an optimum design is 1. The sensitivity isotropy comparison of the four six-axis accelerometers is shown in Table 3.

$$S_{\sigma 1} = \frac{[S_a]_{\min}}{[S_a]_{\max}}, \quad S_{\sigma 2} = \frac{[S_\alpha]_{\min}}{[S_\alpha]_{\max}} \tag{35}$$

Table 3 Sensitivity isotropy comparison of the four six-axis accelerometers

Configurations		6-UPS	7-UPS	8-UPS	9-UPS
S_a components /nc/g	S_{ax}	4.665	5.332	2.905	3.873
	S_{ay}	5.204	3.486	3.486	3.873
	S_{az}	3.486	3.653	2.905	3.873
Linear acceleration isotropy value /$S_{\sigma 1}$		0.670	0.654	0.833	1.000
S_α components /pc/rad/s^2	$S_{\alpha x}$	5.332	5.332	3.554	5.332
	$S_{\alpha y}$	5.332	4.327	2.666	5.332
	$S_{\alpha z}$	7.135	5.587	3.554	5.332
Angular acceleration isotropy value /$S_{\sigma 2}$		0.747	0.774	0.750	1.000

Table 3 shows that the structural asymmetry of the 6-UPS, 7-UPS and 8-UPS configurations causes the sensitivity anisotropy, where the 6-UPS configuration acts as the worst configuration. As the topology configurations of the elastic body tend to be symmetric completely, the 9-UPS configuration achieves the optimal sensitivity isotropy performance. It is illustrated that the six-axis accelerometers' sensitivity isotropy is closely related to the structural symmetry.
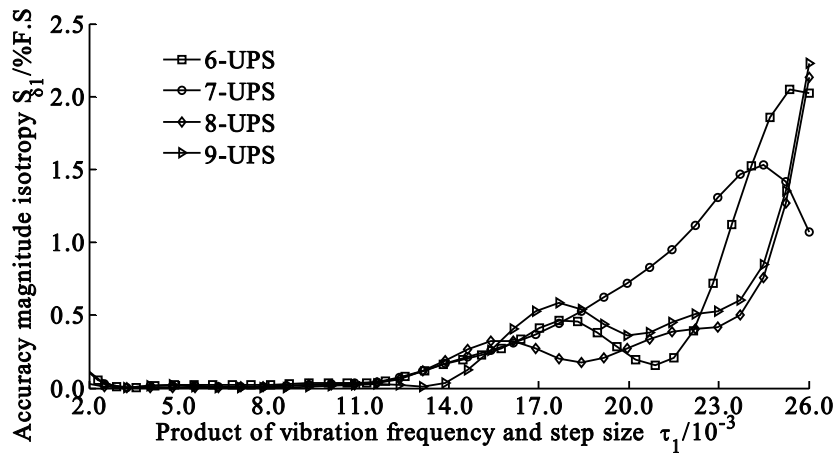
3.4.2 Accuracy Isotropy

The analyses in Sec. 3.1 just denote the numerical error without considering the direction error of the decoupled six-axis acceleration as a vector. Here, accuracy isotropy judged by the standard deviation of the maximal and global fiducial error of the six acceleration components is introduced, which do not reflect how accurate it is, just reflect the principle accuracy consistency, its consistent level, as well as the direction error in decoupling the six-axis acceleration. The optimal case is equal to 0; this index is given by Eqns. 36 and 37 separately.
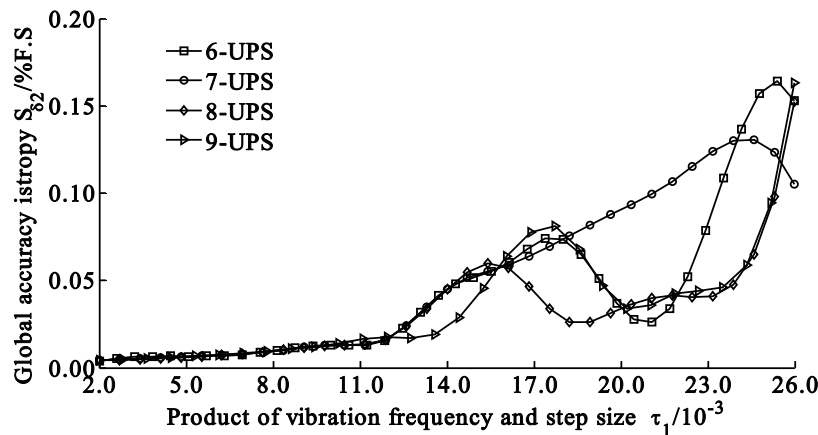
$$S_{\delta 1(3)} = \sqrt{\frac{1}{6}\sum_{i=1}^{6}\left(\left|\gamma_i\right|_{\max} - \delta_{1(3)}\right)^2} \tag{36}$$

$$S_{\delta 2(4)} = \sqrt{\frac{1}{6}\sum_{i=1}^{6}\left(\left|\int_{t_0}^{t_1}\gamma_i \mathrm{d}t\right| - \delta_{2(4)}\right)^2} \tag{37}$$

Without loss of generality, combined with the vibration frequency ranging from 2.0Hz to 26.0Hz and step size ranging from 10^{-5}s to 10^{-2}s discussed in Sec. 3.1 to analyze the accuracy isotropy, the results are depicted in Fig. 7 and Fig. 8, respectively.
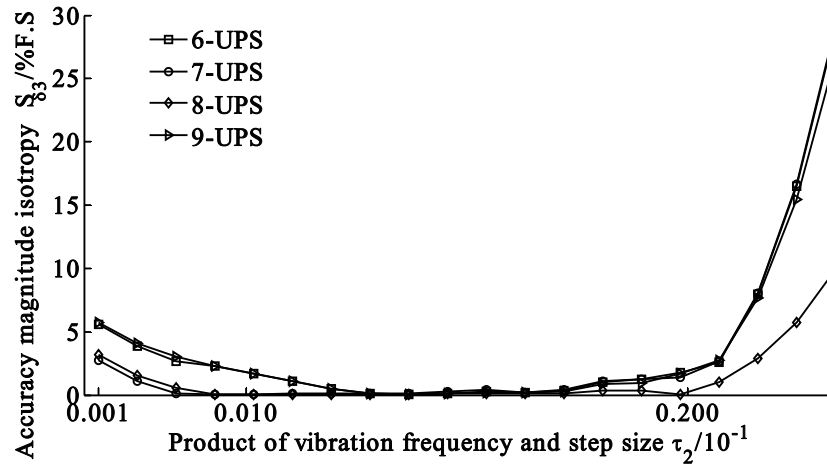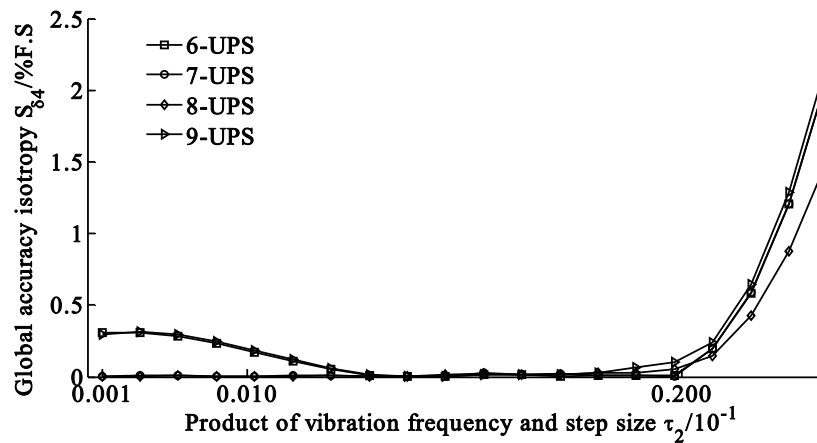

(a) Accuracy magnitude isotropy

(b) Global accuracy isotropy

Fig. 7 The relation between principle accuracy isotropy and vibration frequency of the four six-axis accelerometers

(a) Accuracy magnitude isotropy

(b) Global accuracy isotropy

Fig. 8 The relation between principle accuracy isotropy and step size of the four six-axis accelerometers

The plots in Figs. 7 and 8 clearly show that:

(1) Although the topology configurations of the elastic body, from 6-UPS to 9-UPS, tend to be completely symmetric gradually, the principle accuracy of all the four parallel type six-axis accelerometers cannot meet isotropy, which is caused by the strongly coupled dynamics equations (Eqns. 23). From the vibration frequency aspect, the accuracy isotropy keeps in the same level substantially, while from the step size perspective, the 8-UPS configuration gets a better accuracy isotropy performance, which indicates that the accuracy isotropy is just related to the decoupling algorithm itself.

(2) The carrier's vibration frequency would not affect a certain six-axis accelerometer's principle accuracy isotropy significantly, but the accuracy isotropy decreases with the vibration frequency increasing, which is caused by the unsynchronizing change rate in principle accuracy of the six acceleration components, where the angular acceleration obtains a better precision retentivity in simulations.

(3) Just like the influences of step size on principle accuracy discussed in Sec. 3.1 (2), there also exists an appropriate interval of step size that is $[2 \times 10^{-4}, 1.5 \times 10^{-2}]$s in this simulation, in which the four parallel type six-axis accelerometers can get an optimal accuracy isotropy performance synchronously.

3.5   Working frequency range

To avoid the structural damage caused by the resonance in actual working conditions, as well as to determine the working frequency range of the researched four six-axis accelerometers, it is necessary to carry out the modal analyses on each configuration. Furthermore, since the electric charges developed in the piezoelectric ceramics when mechanical stress is exerted on them are extremely weak, the six-axis accelerometers can only work in cooperation with a charge amplifier. Therefore, its low-frequency response is limited by the lower cut-off frequency of the charge amplifier (can generally reach as low as 0.3Hz), while the upper frequency limit only takes about 1/3 to 1/5 of the first-order natural frequency of the six-axis accelerometer in general [9]. Here, the modal analysis was conducted by the use of ADAMS. The results are shown in Table 4.

Table 4 Working frequency range comparison of the four six-axis accelerometers

Configurations	First-order natural frequency /Hz	Working frequency range /Hz
6-UPS	1662.7	0.3~554.2
7-UPS	1970.1	0.3~657.7
8-UPS	3480.8	0.3~1280.3
9-UPS	2545.8	0.3~848.6

Analysis of Table 4 shows that:

(1) The increase in limbs can improve the first-order natural frequency of the parallel type six-axis accelerometers effectively, thus broadening its working frequency range.

(2) Compared with the first three configurations, the 9-UPS six-axis accelerometer's working bandwidth is greatly shortened, which resulted from the reconfiguration of 9 limbs. It is validated that adopting the layout like the 8-UPS's in 9-UPS configuration will make the upper frequency limit reach 1329.8Hz. Thus, the layout of the limbs determines the accelerometers working bandwidth to some extent.

(3) Combined with the conclusion (2) in Sec. 3.3, it is clear that a proper number of limbs with a reasonable spatial distribution will effectively improve the contradictory relation between the sensitivity and stiffness characteristics of the six-axis accelerometers.

4.   Conclusions

(1) The researched four configurations of parallel type six-axis accelerometer have a closed-form solution of the forward kinematics which lays a theoretical foundation for the dynamics to achieve the real-time decoupling. Based on the quasi-velocities method of Kane's dynamics, a decoupling algorithm was derived in configuration space, which can realize the calculation of the six-axis acceleration completely and timely by the use of numerical methods.

(2) The performances of the four six-axis accelerometers corresponding to different configurations were evaluated through computer simulations. The results give a quantitative comparison on some static characteristics which are directly affected by the configurations, as shown in Table 5.

Table 5 The quantitative comparison of some static characteristics of the four six-axis accelerometers

Configu-rations	Principle accuracy		Efficiency	Sensitivity		Accuracy isotropy		Sensitivity isotropy		Frequency range	Base frequency
	Max	Global		S_a	S_α	Max	Global	$S_{\sigma 1}$	$S_{\sigma 2}$		
6-UPS	0.549	0.299	0.623	1.000	1.000	0.331	0.563	0.670	0.747	0.433	0.433
7-UPS	0.496	0.227	0.621	0.934	0.857	0.394	0.751	0.654	0.774	0.514	0.514
8-UPS	1.000	0.439	0.749	0.696	0.549	1.000	1.000	0.833	0.750	1.000	1.000
9-UPS	0.736	1.000	1.000	0.870	0.898	0.346	0.519	1.000	1.000	0.663	0.663

Note:
A detailed analysis on the indices given in Table 5 has been carried out in Sec. 3. Here, the values of the optimal indices are transformed to unit 1, while the rest are represented with respect to unit 1. Where the principle accuracy is given based on the maximal allowable acquisition frequency that can guarantee to decouple the six acceleration components timely.

In conclusion, the coupling degree of the configurations corresponding to the four parallel six-axis accelerometers will directly determine the construction of an efficient computational algorithm, as well as the real-time decoupling characteristic of the six acceleration components. The number of limbs with a reasonable spatial distribution can effectively improve the contradictory relation between the six-axis accelerometers sensitivity and its stiffness characteristics. The degree of structural symmetry determines the sensitivity isotropy, while the principle accuracy and its isotropy will not be affected by the configurations, which are just closely related to the algorithm itself, especially the step size. According to Table 5, take the 6-UPS as an example, which has the most optimal sensitivity characteristic but with a low principle accuracy and frequency range. These properties allow it to be used in the occasions requiring a less accuracy and narrow-band measurement but a high sensitivity.

(3) The principle accuracy of the studied four parallel type six-axis accelerometers is negatively affected by the carrier's vibration frequency. Such a trend can be improved by increasing the data acquisition frequency or improving the decoupling algorithm. However, due to the inherent properties of the algorithm, this negative effect cannot be eliminated timely and effectively at present. In future, more advanced decoupling algorithm can be adopted to ameliorate this adverse trend.

Additionally, this paper studied four parallel type six-axis accelerometers in principle without considering the influences of signal noise and model error on the estimation. In practice, there are two prerequisites for achieving the measurement of the six-axis acceleration, the first is the preprocessing of output signals from piezoelectric ceramics, including digital filtering, trend term eliminating and outliers rejecting, etc., and the second is the related parameters identification of physical prototype in advance, which will be studied in the future papers.

ACKNOWLEDGMENTS

REFERENCES

[1]   D.H. Wang, G. Yuan: *A six-degree-of-freedom acceleration sensing method based on six coplanar single-axis accelerometers*. IEEE Transactions on Instrumentation and Measurement **60**, no. 2, 1433-1442 (2011).

[2]   E. Edwan, S. Knedlik, O. Loffeld: *Constrained angular motion estimation in a gyro-free IMU*. IEEE transactions on aerospace and electronic systems **47**, no. 1, 596-610 (2011).

[3]   S. Park, C.W. Tan, J. Park: *A scheme for improving the performance of a gyroscope-free inertial measurement unit*. Sensors and Actuators A: Physical **121**, no. 2, 410-420 (2005).

[4]   P. Cardou, J. Angeles: *A comparative study of all- accelerometer strapdowns for UAV INS*. Advanced sensors payloads for UAV. RTO-MP-SET-092, Technical Report **9** (2005).

[5]   V. Chapsky, V.T. Portman, B.Z. Sandler: *Single-mass 6-dof isotropic accelerometer with segmented PSD sensors*. Sensors and Actuators A : Physical **135**, no. 2, 558-569 (2007).

[6]   M. Meng, Z.C. Wu, Y. Yu, Y. Ge, Y.J. Ge: *Design and characterization of a six-axis accelerometer*. Proceedings-IEEE International Conference on Robotics and Automation, Barcelona, 2005: vol. 2005, 2356-2361.

[7]   R. Amarasinghe, D.V. Dao, T. Toriyama: *Design and fabrication of a miniaturized six-degree-of-freedom piezoresistive accelerometer*. Journal of Micromechanics and Microengineering **15**, 1745-1753 (2005).

[8]   C.Z. Yu, X.Y. Zhang, J.H. Han, L.C. Tian: *Study on static characteristics of an integrated six-axis accelerometer based on parallel mechanism*. Advanced Materials Research **129**, 224-229 (2010).

[9]   J.J. You: *Research on a piezoelectric six-axis accelerometer based on 6-SPS parallel mechanism*. M.E. thesis, College of Mechanical and Electrical Engineering, Nanjing university of Aeronautics and Astronautics, 83 pp, 2009 (in Chinese).

[10]   J.J. You, C.G. Li, H.T. Wu: *Research on Hamiltonian dynamics of parallel type six-axis accelerometer*. Journal of Mechanical Engineering **48**, no. 15, 9-17 (2012). (in Chinese).

[11]   S.K. Song, D.S. Kwon: *A tetrahedron approach for a unique close-form solution of the forward kinematics of six-dof parallel mechanisms with multiconnected joints*. Journal of Robotic systems **19**, no. 6, 269-281 (2002).

[12]   M. Möller, C. Glocker: *Rigid body dynamics with a scalable body, quaternions and perfect constraints*. Multibody System Dynamics **27**, no. 4, 437-454 (2012).

[13]   J. R. Dooley, J.M. Mccarthy: *Spatial rigid body dynamics using dual quaternion components*. Proceedings-IEEE international conference on robotics and automation, California, 1991: vol, 1, 90-95.

[14]   T.R. Kane, D.A. Levison: *The use of Kane's dynamical equations in robotics*. The international journal of robotics research **2**, no. 3, 3-21 (1983).

[15]   A.H. Bajodah, D.H. Hodges, Y.H. Chen: *Nonminimal Kane's equations of motion for multibody dynamical systems subject to nonlinear nonholonomic constraints*. Multibody Systems Dynamics **14**, no. 2, 155-187 (2005).

[16]   R.D. Hampton: *A finite-patch model of a flexible plate via Kane's dynamics*. International journal of vehicle systems modeling and testing **7**, no. 4, 303-350 (2012).

[17]   R. Featherstone: *Rigid body dynamics algorithms*. Springer science+Business media LLC, New York, 2008.

Xia Yuhui
Li Chenggang
You Jingjing
Shen Jingjin
College of Mechanical and Electrical
Engineering
Nanjing University of Aeronautics and
Astronautics
Yudao str. 29
210016 Nanjing, China
Tel: +86-15251870313;
E-mail: xiayuh1314@163.com
        lichenggang@nuaa.edu.cn
Jason Zachary Moore
Department of Mechanical and Nuclear
Engineering
The Pennsylvania State University
University Park, 16802, Pennsylvania USA